

# E2Former-V2: On-the-Fly Equivariant Attention with Linear Activation Memory

Lin Huang<sup>\*1</sup> Chengxiang Huang<sup>\*1,2</sup> Ziang Wang<sup>1</sup> Yiyue Du<sup>3</sup> Chu Wang<sup>1,4</sup> Haocheng Lu<sup>1,5</sup> Yunyang Li  
Xiaoli Liu<sup>1</sup> Arthur Jiang<sup>1</sup> Jia Zhang<sup>1</sup>

## Abstract

Equivariant Graph Neural Networks (EGNNs) have become a widely used approach for modeling 3D atomistic systems. However, mainstream architectures face critical scalability bottlenecks due to the explicit construction of geometric features or dense tensor products on *every* edge. To overcome this, we introduce **E2Former-V2**, a scalable architecture that integrates algebraic sparsity with hardware-aware execution. We first propose **Equivariant Axis-Aligned Sparsification (EAAS)**. EAAS builds on Wigner-6j convolution by exploiting an  $SO(3) \rightarrow SO(2)$  change of basis to transform computationally expensive dense tensor contractions into efficient, sparse parity re-indexing operations. Building on this representation, we introduce **On-the-Fly Equivariant Attention**, a fully node-centric mechanism implemented via a custom fused Triton kernel. By eliminating materialized edge tensors and maximizing SRAM utilization, our kernel achieves a **20 $\times$  improvement in TFLOPS** compared to standard implementations. Extensive experiments on the SPICE and OMol25 datasets demonstrate that E2Former-V2 maintains comparable predictive performance while notably accelerating inference. This work demonstrates that large equivariant transformers can be trained efficiently using widely accessible GPU platforms. The code is available at <https://github.com/IQuestLab/UBio-MolFM/tree/e2formerv2>.

## 1. Introduction

Machine learning techniques have gained increasing popularity in atomistic modeling (Bartók et al., 2013; 2010;

<sup>1</sup>IQuest Research <sup>2</sup>UNSW Sydney <sup>3</sup>Tsinghua University  
<sup>4</sup>Zhejiang University <sup>5</sup>Peking University. Correspondence to: Jia Zhang <jialrs.z@iquestlab.com>.

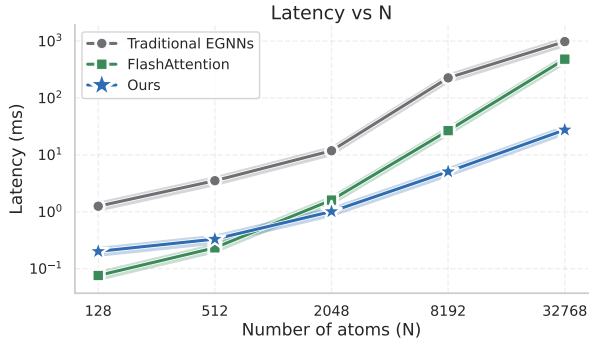


Figure 1. **Latency vs. number of atoms ( $N$ ) for Traditional EGNNs, FlashAttention, and Ours.** FlashAttention consistently improves over Traditional EGNNs across all system sizes. The advantage of our method becomes increasingly pronounced as  $N$  grows. See Appendix A for detailed experimental settings.

Drautz, 2019). These methods offer significantly higher efficiency compared to quantum mechanical approaches, such as Density Functional Theory (DFT) (Hohenberg & Kohn, 1964; Kohn & Sham, 1965), while maintaining comparable performance. In this domain, *equivariant graph neural networks* have emerged as a promising class of models, as they preserve the rotational and translational symmetries required for physically meaningful predictions (Schütt et al., 2018; Gasteiger et al., 2021; Geiger et al., 2022; Unke et al., 2021; Liao & Smidt, 2023).

Recent architectures such as eSCN (Passaro & Zitnick, 2023), ViSNet (Wang et al., 2022), EquiformerV2 (Liao et al., 2023), GotenNet (Aykent & Xia, 2025), eSEN (Fu et al., 2025), E2Former (Li et al., 2025), and UMA (Wood et al., 2025) use rich geometric representations and expressive message passing. These design choices lead to notable performance improvements. Despite their differing mathematical formulations, these models share a common characteristic: **their computation and memory footprint are inherently edge-centric**. In practice, they explicitly construct geometric features or perform tensor products on *every* edge. With typical neighbor counts ( $k \approx 30$ – $100$ ), edge-centric message passing and attention incur activation and memory costs that remain  $\mathcal{O}(|\mathcal{E}|)$ ; for molecular graphs with bounded degree (e.g.,  $k$ -NN or radius cutoff),  $|\mathcal{E}| \approx kN$ , i.e.,  $\mathcal{O}(|\mathcal{E}|) = \mathcal{O}(kN)$ .

To quantify the impact of this design, we conducted an observational analysis comparing these traditional EGNNs against standard attention mechanisms. As illustrated by the gray line in Figure 1, traditional EGNNs suffer from severe latency due to their edge-centric nature. In contrast, standard Transformers have overcome similar bottlenecks through *hardware-aligned execution* and SRAM-optimized kernels (Dao et al., 2022; Dao, 2023; Shah et al., 2024). FlashAttention (Dao et al., 2022), represented by the green line in Figure 1, computes attention in a streaming, tile-based manner. This avoids materializing the full attention matrix, reducing activation memory from  $\mathcal{O}(N^2)$  to  $\mathcal{O}(N)$  and bridging the gap between GPU compute throughput and off-chip memory bandwidth.

To the best of our knowledge, these execution principles remain unexplored in existing  $SO(3)$ -equivariant architectures. This poses a fundamental question: *can equivariant attention be reformulated to support SRAM-optimized, streaming execution?* Such a formulation would eliminate explicit edge activations, ensuring memory complexity remains linear with the number of atoms.

We demonstrate that this is achievable with **E2Former-V2**, a fully node-centric architecture that brings FlashAttention-style streaming computation to equivariant models. As shown by the blue line in Figure 1, our approach significantly alleviates the aforementioned bottlenecks. Significantly, this performance gain widens as  $N$  increases, underscoring E2Former-V2’s efficacy in handling large-scale atomic structures that were previously computationally prohibitive.

E2Former-V2 achieves  $\mathcal{O}(|\mathcal{V}|)$  activation memory while preserving theoretical exactness by leveraging two core designs: an  $SO(2)$  rotational basis for sparsification and a custom equivariant attention kernel. **Firstly**, we propose **Equivariant Axis-Aligned Sparsification (EAAS)**. Inspired by the eSCN (Passaro & Zitnick, 2023), which rotates features to an  $SO(2)$  frame to sparsify Clebsch–Gordan coefficients, we integrate this strategy with Wigner-6j recoupling identities. This combination allows the expensive full  $SO(3)$  convolution to be implemented as a re-indexing of  $SO(2)$  modes via simple blockwise linear maps. **Secondly**, we introduce our **On-the-Fly Equivariant Attention**. Unlike traditional methods that materialize explicit edge tensors, our kernel computes interaction influence via a custom fused Triton kernel that maximizes SRAM utilization. Our contribution could be summarized as follows:

1. **Equivariant Axis-Aligned Sparsification (EAAS).** We unify Wigner-6j recoupling with  $SO(2)$  sparsification, transforming dense tensor contractions into sparse parity re-indexing operations. The result is a  $\sim 6\times$  speedup during the convolution stage.

2. **On-the-Fly Equivariant Attention.** We propose a fully fused attention kernel that avoids  $\mathcal{O}(|\mathcal{E}|)$  memory materialization. By leveraging tiling and recomputation, this design eliminates the primary memory bottleneck of geometric graphs and achieves a  $20\times$  improvement in TFLOPS compared to standard implementations.
3. Extensive experiments on large-scale molecular benchmarks demonstrate that E2Former-V2 achieves superior performance. Furthermore, it significantly outperforms related methods in training throughput and memory efficiency, validating the scalability of E2Former-V2.

## 2. Related Work

**Equivariant graph neural networks.** Equivariant graph neural networks (GNNs) have become a central paradigm for modeling 3D geometric data. Early works emphasized computational efficiency by restricting representations to scalars and vectors ( $L \leq 1$ ). Methods such as EGNN (Satorras et al., 2022), PaiNN (Schütt et al., 2021), and Allegro (Musaelian et al., 2022) avoid explicit tensor products, achieving linear complexity in graph size. While efficient, this restriction limits their ability to model higher-order angular correlations encoded in spherical harmonics.

To improve expressivity, Tensor Field Networks (TFN) (Thomas et al., 2018) and NequIP (Batzner et al., 2022) introduced full  $SO(3)$ -equivariant convolutions based on tensor products. These models significantly enhance angular modeling capacity but incur prohibitive computational costs, scaling as  $\mathcal{O}(L^6)$ . Subsequent works, including eSCN (Passaro & Zitnick, 2023), EquiformerV2 (Liao et al., 2023), and ViSNet (Wang et al., 2022), reduce this complexity to  $\mathcal{O}(L^3)$  by exploiting a change of basis to  $SO(2)$ . Despite these advances, most existing approaches remain *edge-centric*, relying on the explicit construction and storage of edge-wise features.

Recent studies have begun to question whether such edge materialization is fundamentally necessary. Node-centric formulations based on factorized  $SO(3)$  convolutions suggest that equivariant interactions can, in principle, be decomposed into node-wise computations. This reformulation reduces the *theoretical* complexity from  $\mathcal{O}(|\mathcal{E}|)$  to  $\mathcal{O}(|\mathcal{V}|)$ . E2Former (Li et al., 2025) provides an important theoretical foundation by demonstrating the mathematical feasibility of this factorization. However, these reductions in arithmetic complexity do not automatically translate into practical speedups, as memory access patterns and hardware constraints are largely ignored.

**Hardware-Aware Efficient Deep Learning.** In modern GPU architectures, performance is increasingly dominated by memory access rather than floating-point operations (Wulf & McKee, 1995; Williams et al., 2009). While high-

bandwidth memory (HBM) offers large capacity, its bandwidth is orders of magnitude lower than that of on-chip SRAM (Jia et al., 2018). As a result, many deep learning workloads are constrained by memory movement rather than computation (Ivanov et al., 2021).

This issue is particularly severe in spherical GNNs, where large edge-wise tensor products incur substantial HBM traffic (Thomas et al., 2018; Geiger & Smidt, 2022). Even when the arithmetic complexity is reduced, explicitly materializing intermediate tensors can saturate memory bandwidth and limit wall-clock performance (Liao et al., 2023; Passaro & Zitnick, 2023). In contrast, hardware-aware methods such as FlashAttention (Dao et al., 2022; Shah et al., 2024) demonstrate that careful kernel fusion and tiling strategies can substantially reduce memory I/O by keeping intermediate results in SRAM.

Despite their success in Transformers, extending such hardware-aware optimization techniques to equivariant GNNs remains largely unexplored. The irregular structure of graphs (Fey & Lenssen, 2019) and the complexity of spherical harmonic operations pose unique challenges, leaving a significant gap between algorithmic factorization and practical hardware-efficient realization.

### 3. Preliminaries

We introduce the notation and mathematical background of  $\text{SO}(3)$ -equivariant graph neural networks, and briefly review the node-centric factorization proposed in E2Former (Li et al., 2025), which serves as the theoretical foundation of our method.

**Graph and representations.** We consider a molecular graph  $\mathcal{G} = (\mathcal{V}, \mathcal{E})$  with  $N = |\mathcal{V}|$  nodes. Each node  $i$  is associated with a 3D coordinate  $\vec{r}_i \in \mathbb{R}^3$  and a feature representation  $\mathbf{h}_i$ . Relative positions are defined as  $\vec{r}_{ij} = \vec{r}_j - \vec{r}_i$ .

Node features are modeled as a direct sum of irreducible representations (irreps) of  $\text{SO}(3)$ :

$$\mathbf{h}_i = \bigoplus_{\ell=0}^L \mathbf{h}_i^{(\ell)}, \quad \mathbf{h}_i^{(\ell)} \in \mathbb{R}^{C_\ell \times (2\ell+1)}. \quad (1)$$

Under a rotation  $R \in \text{SO}(3)$ , features of degree  $\ell$  transform as  $\mathbf{h}_i^{(\ell)} \mapsto D^{(\ell)}(R)\mathbf{h}_i^{(\ell)}$ , where  $D^{(\ell)}$  denotes the Wigner- $D$  matrix.

**Geometric encoding.** Geometric information is encoded using *solid spherical harmonics*  $\mathcal{R}^{(\ell)}(\vec{r}) \in \mathbb{R}^{2\ell+1}$ , defined as

$$\mathcal{R}_m^{(\ell)}(\vec{r}) = \|\vec{r}\|^\ell Y_{\ell,m}\left(\frac{\vec{r}}{\|\vec{r}\|}\right), \quad (2)$$

where  $Y_{\ell,m}$  are real spherical harmonics.

**Equivariant tensor product.** We denote by  $\otimes$  the Clebsch–Gordan tensor product, which is a bilinear map between irreducible representations of  $\text{SO}(3)$ . In the following derivation, we omit the parity for notational simplicity. Given two irreps  $\mathbf{u}^{(\ell_1)}$  and  $\mathbf{v}^{(\ell_2)}$ , their coupling to an output irrep of degree  $\ell_{\text{out}}$  is defined as:

$$\left(\mathbf{u}^{(\ell_1)} \otimes \mathbf{v}^{(\ell_2)}\right)_m^{(\ell_{\text{out}})} = \sum_{m_1, m_2} C_{\ell_1, m_1; \ell_2, m_2}^{\ell_{\text{out}}, m} u_{m_1}^{(\ell_1)} v_{m_2}^{(\ell_2)}, \quad (3)$$

where  $C_{\dots}$  are the Clebsch–Gordan coefficients.

**E2Former: node-centric factorization.** E2Former (Li et al., 2025) reformulates spherical convolution by algebraically factorizing the tensor product between node features and relative geometric encodings. Specifically, it considers an attention-weighted aggregation of edge messages:

$$\mathbf{m}_i = \sum_{j \in \mathcal{N}(i)} \alpha_{ij} \mathbf{m}_{ij}, \quad (4)$$

where  $\alpha_{ij}$  is a scalar coefficient and each edge message is defined as  $\mathbf{m}_{ij} = \mathbf{h}_j \otimes \mathcal{R}^{(\ell)}(\vec{r}_{ij})$ .

Using the Binomial Local Expansion theorem together with Wigner-6j recoupling, E2Former shows that the tensor product involving the relative position  $\vec{r}_{ij} = \vec{r}_j - \vec{r}_i$  can be decomposed into a sum of terms that separately depend on the source node  $j$  and the target node  $i$ . The resulting factorized form is given by:

$$\mathbf{m}_i^{(\ell_{\text{out}})} = \sum_{u=0}^{\ell} (-1)^{\ell-u} \binom{\ell}{u} \left[ \underbrace{\mathcal{R}^{(u)}(\vec{r}_i)}_{\text{Target Node}} \otimes_{6j} \left( \sum_{j \in \mathcal{N}(i)} \alpha_{ij} \cdot \underbrace{\left( \mathbf{h}_j \otimes \mathcal{R}^{(\ell-u)}(\vec{r}_{ij}) \right)}_{\text{Source Node}} \right) \right]^{(\ell_{\text{out}})}. \quad (5)$$

In Eq. (5), the inner summation aggregates source-node features  $\mathbf{h}_j$  coupled with their absolute geometric encodings  $\mathcal{R}^{(\ell-u)}(\vec{r}_j)$ . The outer tensor product combines this aggregated source representation with a target-node-dependent geometric factor  $\mathcal{R}^{(u)}(\vec{r}_i)$ . The operator  $\otimes_{6j}$  denotes an  $\text{SO}(3)$ -equivariant recoupling where the path weight is parameterized by Wigner-6j recoupling coefficients.

## 4. Method

### 4.1. Motivation for E2Former-V2.

Despite the theoretical elegance of Eq. (5), practical implementation encounters two bottlenecks. **Firstly**, the equivariant tensor contractions, including both standard CG-products ( $\otimes$ ) and their Wigner-6j counterparts ( $\otimes_{6j}$ ), traverse dense Clebsch–Gordan paths and incur  $O(L^6)$  computational complexity. This creates a notable computational

overhead when scaling to higher  $L$ . **Secondly**, E2Former achieves decoupling only at the level of convolutional message computation; the scalar attention weight  $\alpha_{ij}$  remains edge-dependent. Standard automatic differentiation frameworks materialize these weights as an  $\mathcal{O}(|\mathcal{E}|)$  tensor in High Bandwidth Memory (HBM), which reintroduces a memory wall for large-scale systems.

We propose **E2Former-V2**, a unified equivariant architecture designed to realize the theoretical promise of linear-scaling learning. While the node-centric factorization (Eq. 5) theoretically eliminates edge complexity, existing realizations remain constrained by two fundamental bottlenecks: the *arithmetic intensity* of **dense SO(3) tensor contractions**, and the *memory wall* of implicit edge instantiations. Our method overcomes these barriers through a holistic design shown in figure 2 that combines an algebraic  $\text{SO}(3) \rightarrow \text{SO}(2)$  reduction with hardware-aware computing.

#### 4.2. Atom-level equivariant attention.

Our attention mechanism serves as the architectural realization of the node-centric factorization derived in Section 3. Instead of treating edge features as first-class tensors, we design a computational pipeline that strictly confines geometric information to the node-wise value path.

**Equivariant feature projection.** To preserve the  $\text{SO}(3)$  symmetry of the input features  $\mathbf{h}_i$ , we enforce that all learnable transformations commute with the group action. We achieve this by applying block-diagonal linear projections independently to each irreducible subspace. Let  $W_Q = \text{diag}_\ell W_Q^{(\ell)}$  and  $W_K = \text{diag}_\ell W_K^{(\ell)}$ . We realize per- $\ell$  query and key parts as:

$$\begin{aligned} \mathbf{q}_i &= \text{concat}_{\ell=0}^L \left( W_{Q1}^{(\ell)} \mathbf{h}_i^{(\ell)} \parallel (W_{Q2}^{(\ell)} \mathbf{h}_i^{(\ell)})^\top \right), \\ \mathbf{k}_j &= \text{concat}_{\ell=0}^L \left( W_{K1}^{(\ell)} \mathbf{h}_j^{(\ell)} \parallel (W_{K2}^{(\ell)} \mathbf{h}_j^{(\ell)})^\top \right), \end{aligned} \quad (6)$$

The features  $\mathbf{h}_j$  used in the message path are similarly projected within each  $\ell$ -block using a learnable matrix  $W_H^{(\ell)}$ . Because each block-diagonal transformation commutes with  $D^{(\ell)}$ , these features transform equivariantly. This establishes the necessary conditions for invariant scoring.

**Implicit invariant scoring.** With features prepared, we construct the attention weights  $\alpha_{ij}$ . Since standard dot products are not rotationally invariant, we compute scalar scores by aggregating inner products, augmented by a geometric bias:

$$\alpha_{ij} = \text{softmax}_{j \in \mathcal{N}(i)} \left( \frac{1}{\sqrt{d_k}} \mathbf{q}_i^\top \mathbf{k}_j + b(r_{ij}) \right) \cdot \phi(r_{ij}). \quad (7)$$

Critically, this scalar  $\alpha_{ij}$  represents the **only** edge-dependent term in our architecture. By design, it carries no angular momentum and consumes minimal memory.

**Implementation of factorized message passing.** We realize the factorization theorem shown in Eq. 5 as a three-stage data flow. This design ensures that directional information enters only on the value path, strictly decoupling edge interactions:

- (i) **Source-term preparation.** Before message passing, we pre-couple the value features  $\mathbf{v}_j$  with local spherical harmonics at the source node. This operation depends solely on node  $j$ :

$$\mathbf{h}'_j = \mathbf{h}_j \otimes \mathcal{R}(\vec{r}_j). \quad (8)$$

- (ii) **Weighted aggregation.** We transmit these pre-computed terms using the scalar attention weights  $\alpha_{ij}$ . We define the aggregated spatial message  $\mathbf{m}_i$  as the weighted sum of neighbor source terms:

$$\mathbf{m}_i = \sum_{j \in \mathcal{N}(i)} \alpha_{ij} \cdot \mathbf{h}'_j. \quad (9)$$

Unlike standard messages,  $\mathbf{m}_i$  aggregates geometric information without yet resolving the target orientation.

- (iii) **Target-term coupling.** Finally, the aggregated message  $\mathbf{m}_i$  is coupled with the target node’s spherical harmonics  $\mathcal{R}(\vec{r}_i)$  to recover the full equivariant update  $\hat{\mathbf{h}}_i$ :

$$\hat{\mathbf{h}}_i = \mathbf{m}_i \otimes \mathcal{R}(\vec{r}_i). \quad (10)$$

#### 4.3. Equivariant Axis-Aligned Sparsification (EAAS)

The primary computational challenge in node-centric architectures arises from the dense tensor products required in Eq. 8 and Eq. 10. To resolve this arithmetic bottleneck, We introduce **Equivariant Axis-Aligned Sparsification (EAAS)**, an algebraic reduction that converts dense  $\text{SO}(3)$  tensor products into sparse, permutation-based operations while preserving *exact* equivariance.

At a high level, EAAS exploits the fact that geometric encodings become maximally sparse when expressed in a local, axis-aligned frame. By commuting rotations through the tensor product, dense couplings collapse into a fixed re-indexing rule followed by lightweight blockwise linear maps.

**Lemma 4.1** (Pole Sparsity of Solid Spherical Harmonics). *Let  $R \in \text{SO}(3)$  be a rotation that aligns the global  $z$ -axis with a vector  $\vec{r}$ . Then the solid spherical harmonics satisfy*

$$\mathcal{R}_m^{(\ell)}(R\vec{r}) \propto \delta_{m,0}. \quad (11)$$

Lemma 4.1 implies that geometric features become maximally sparse in the aligned frame, providing the key ingredient for eliminating dense summation over magnetic indices. Motivated by this observation, we introduce an alignment



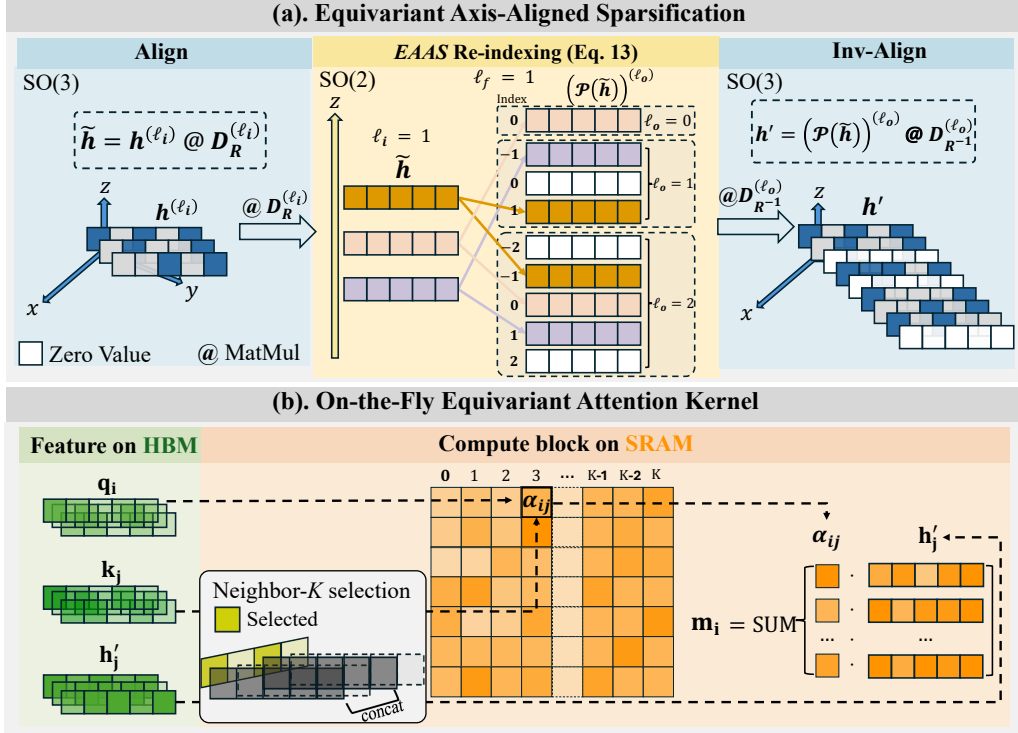


Figure 2. **Key components of E2Former-V2.** (a) **EAAS.** E2Former-V2 aligns features with  $D_R$ , applies the sparse EAAS re-indexing operator  $\mathcal{P}$  (Eq. 13) in the axis-aligned frame, and inverse-aligns with  $D_{R^{-1}}$ . The visualization shows the re-indexing pattern for  $\ell_i = 1$  and  $\ell_f = 1$ . (b) **On-the-fly equivariant attention.** E2Former-V2 computes attention by streaming over neighbors and accumulating the output on the fly, avoiding explicit materialization of edge-level intermediates.

rotation  $R$  and its corresponding representation matrices  $D_R^{(\ell)}$ , which map features from the global  $\text{SO}(3)$  frame into the local axis-aligned frame. We write the aligned node features as

$$\tilde{h} := h^{(\ell_i)} @ D_R^{(\ell_i)}, \quad (12)$$

where  $@$  denotes matrix multiplication.

**Definition 4.2** (EAAS Re-indexing Operator). Let  $\tilde{h}$  denote node features expressed in the aligned frame. We define the *re-indexing operator*  $\mathcal{P}$  as the blockwise linear map (acting independently on each degree  $\ell$ ) whose componentwise action is given by

$$(\mathcal{P}(\tilde{h}))_{m_o}^{(\ell_o)} := \begin{cases} C_{(\ell_i, m_i), (\ell_f, 0)}^{(\ell_o, m_o)} \tilde{h}_{m_i}^{(\ell_i)}, & \text{if } L_\Sigma \text{ is even,} \\ -2(-1)^{m_o} C_{(\ell_i, -m_i), (\ell_f, 0)}^{(\ell_o, m_o)} \tilde{h}_{-m_i}^{(\ell_i)}, & \text{if } L_\Sigma \text{ is odd,} \end{cases}, \quad (13)$$

where  $L_\Sigma = \ell_i + \ell_f + \ell_o$  and  $m_i = m_o$ .

The operator  $\mathcal{P}$  therefore implements a deterministic re-indexing within each  $\ell$ -block, so that for each output order  $m_o$  at most one input order  $m_i$  contributes. This yields a sparse, permutation-like operation and avoids explicitly materializing dense Clebsch–Gordan contraction paths. A complete derivation of the above rule from Clebsch–Gordan coefficients, including the parity selection and sign convention, is provided in Appendix B.

**Proposition 4.3** (Equivariant Axis-Aligned Sparsification). Let  $R \in \text{SO}(3)$  align the  $z$ -axis with  $\vec{r}$ . The  $\text{SO}(3)$ -equivariant tensor product between node features  $h^{(\ell_i)}$  and geometric encoding  $\mathcal{R}^{(\ell_f)}(\vec{r})$  admits the exact form

$$(h^{(\ell_i)} \otimes \mathcal{R}^{(\ell_f)}(\vec{r}))_{m_o}^{(\ell_o)} = (\mathcal{P}(\tilde{h}))^{(\ell_o)} @ D_{R^{-1}}^{(\ell_o)}, \quad (14)$$

where the repeated index  $m_i$  is implicitly summed over.

Proposition 4.3 shows that dense  $\text{SO}(3)$  tensor products can be implemented via rotation conjugation and a sparse, blockwise re-indexing operator. A complete derivation of Proposition 4.3, including the parity selection rules and concrete low-degree examples, is given in Appendix B.

#### 4.4. On-the-Fly Equivariant Attention

This section presents a fused GPU kernel for computing the equivariant attention aggregation defined in Eq. (9). The kernel is designed to eliminate the explicit materialization of edge-level intermediate tensors by evaluating sparse attention as a node-centric, streaming reduction over neighbors. We use  $H$  to denote the number of attention heads. For clarity, we present the single-head formulation ( $H = 1$ ) and omit the head index; the multi-head case follows by applying the same computation independently per head.

**Neighbor indexing and sparse gather.** We consider a molecular system with  $N$  atoms. For each target atom  $i$ ,

let  $\mathcal{N}(i) = \{j_1, \dots, j_{K_i}\}$  denote its neighbor set, where  $K_i \leq K$  and  $K$  represents the maximum number of neighbors permitted per atom. This sparse adjacency structure is encoded by an integer index tensor  $\mathbf{I} \in \mathbb{Z}^{N \times K}$ , where  $\mathbf{I}_{ik} = j_k$  stores the global index of the  $k$ -th neighbor of atom  $i$ .

The index tensor  $\mathbf{I}$  induces an implicit gather operation from node-indexed features to neighbor-indexed features. Given queries and keys  $q, k \in \mathbb{R}^{N \times d}$  and the source-term features  $h' \in \mathbb{R}^{N \times C}$ , the expressions  $k_{\mathbf{I}_{ik}}$  and  $h'_{\mathbf{I}_{ik}}$  correspond to indirect memory accesses. These gathers are performed dynamically inside the kernel and are never materialized as dense tensors of shape  $N \times K \times d$  or  $N \times K \times C$ .

**Streaming node-centric formulation.** The proposed kernel evaluates the aggregation in Eq. (9) as a streaming reduction. As shown in Algorithm 1, rather than computing all scores in advance, the kernel iterates over neighbors  $k \in \{1, \dots, K\}$  and evaluates each inner product on the fly. To ensure numerical stability, we use an online softmax formulation. For each atom  $i$ , the kernel maintains a running maximum  $\mu_i$ , a normalization accumulator  $z_i$ , and a value accumulator  $\mathbf{A}_i \in \mathbb{R}^C$ :

$$\mu_i^{(k)} = \max(\mu_i^{(k-1)}, s_{ij}), \quad (15)$$

$$z_i^{(k)} = z_i^{(k-1)} \exp(\mu_i^{(k-1)} - \mu_i^{(k)}) + \exp(s_{ij} - \mu_i^{(k)}), \quad (16)$$

$$\mathbf{A}_i^{(k)} = \mathbf{A}_i^{(k-1)} \exp(\mu_i^{(k-1)} - \mu_i^{(k)}) + \exp(s_{ij} - \mu_i^{(k)}) \phi(r_{ij}) \mathbf{h}'_j, \quad (17)$$

where  $j = \mathbf{I}_{ik}$  and  $\mathbf{h}'_j$  is the source-term feature for node  $j$ . The unnormalized score  $s_{ij}$  is recalled from Eq. (7):

$$s_{ij} = \frac{1}{\sqrt{d_k}} q_i^\top k_j + b(r_{ij}). \quad (18)$$

After all neighbors are processed, the final aggregated message for the head is  $m_i = \mathbf{A}_i^{(K)} / z_i^{(K)}$ .

**Memory and performance implications.** By avoiding the explicit materialization of the attention scores  $\alpha_{ij}$  and the gathered value tensors, the fused kernel eliminates the dominant sources of intermediate memory allocation and HBM traffic in sparse attention. All reductions over the neighbor dimension are performed on chip, and each key and value vector is loaded exactly once per interaction. As a result, the computation shifts from being memory-bound to compute-bound, substantially improving throughput and enabling equivariant attention to scale to large molecular systems.

**Algorithm 1** Fused On-the-Fly Equivariant Attention (Forward Pass,  $H = 1$ )

**Require:**  $q, k \in \mathbb{R}^{N \times d}$ ,  $h' \in \mathbb{R}^{N \times C}$ , neighbor index  $\mathbf{I} \in \mathbb{Z}^{N \times K}$ , bias  $b(r)$ , radial scaling  $\phi(r)$ , scale  $\tau = 1/\sqrt{d_k}$

**Ensure:** Aggregated message  $m \in \mathbb{R}^{N \times C}$

```

1: for each target atom  $i \in \{1, \dots, N\}$  in parallel do
2:    $\mu \leftarrow -\infty, z \leftarrow 0, \mathbf{A} \leftarrow \mathbf{0}$ 
3:   for  $k = 1$  to  $K$  do
4:      $j \leftarrow \mathbf{I}_{ik}$ 
5:     if  $j$  is padding then
6:       continue
7:     end if
8:      $s \leftarrow \tau \cdot q_i^\top k_j + b(r_{ij})$ 
9:      $\mu' \leftarrow \max(\mu, s)$ 
10:     $z \leftarrow z \cdot e^{\mu - \mu'} + e^{s - \mu'}$ 
11:     $\mathbf{A} \leftarrow \mathbf{A} \cdot e^{\mu - \mu'} + e^{s - \mu'} \cdot \phi(r_{ij}) h'_j$ 
12:     $\mu \leftarrow \mu'$ 
13:   end for
14:    $m_i \leftarrow \mathbf{A} / z$ 
15: end for
    
```

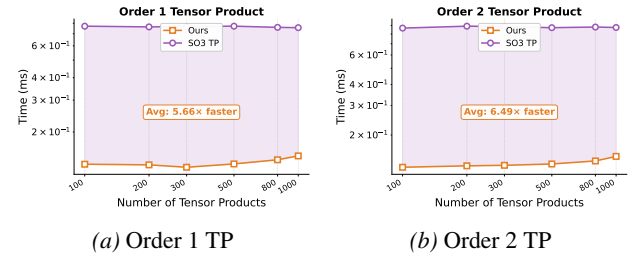


Figure 3. Forward pass time comparison between our EAAS SO(2)-based tensor product and e3nn’s SO(3) tensor product. Benchmarked with  $\ell_{\max} = 2$  and 128 channels across varying numbers of tensor product operations.

## 5. Experiments

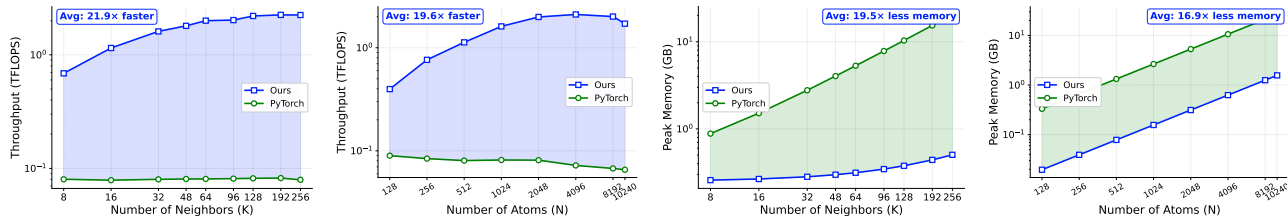
We evaluate E2FormerV2 on standard molecular benchmarks to verify its computational efficiency, scalability, and predictive accuracy. Our experiments aim to confirm that the proposed EAAS and on-the-fly equivariant attention kernel reduce the computational complexity without compromising the model’s expressivity.

### 5.1. Datasets.

We utilize **SPICE** (Eastman et al., 2022) to verify precision in medicinal chemistry contexts (e.g., protein-ligand interactions), and **OMol25** (Levine et al., 2025) to assess high-throughput capabilities across the massive, diverse chemical spaces required for foundation models. Details of the tow datasets are provided in Appendix C.

### 5.2. Efficiency and scalability analysis.

We validate the computational efficiency and scalability of E2Former-V2 from both algebraic and hardware perspectives. **Firstly**, we evaluate the impact of our Equivariant Axis-Aligned Sparsification (EAAS). As illustrated in Fig-



(a) TFLOPS vs. Neighbors (b) TFLOPS vs. Atoms (N) (c) Peak Memory vs. Neighbors (d) Peak Memory vs. Atoms (N)

Figure 4. Performance benchmarks of our on-the-fly equivariant attention kernels on H2O GPU. (a)(b) Computational throughput (TFLOPS) as a function of the number of neighbors  $K$  and atoms  $N$ , respectively. (c)(d) Peak GPU memory usage (GB) as a function of the number of neighbors  $K$  and atoms  $N$ , respectively.

Table 1. Performance comparison on the SPICE dataset. Results are reported in Energy ( $E$ , meV/atom) and Force ( $F$ , meV/Å) MAE. **Bold** and underline denote the best and second-best performers. Shaded rows indicate our proposed method.

MODEL	PUBCHEM		MONOMERS		DIMERS		DIPEPTIDES		SOLV. AMINO		WATER		QMUGS		ALL	
	$E$	$F$	$E$	$F$	$E$	$F$	$E$	$F$	$E$	$F$	$E$	$F$	$E$	$F$	$E$	$F$
MACE Small	1.41	35.68	1.04	17.63	0.98	16.31	0.84	25.07	1.60	38.56	1.67	28.53	1.03	41.45	1.27	29.76
MACE Medium	0.91	20.57	0.63	9.36	0.58	9.02	0.52	14.27	1.21	23.26	<u>0.76</u>	15.27	0.69	23.58	0.80	17.03
MACE Large	0.88	14.75	0.59	6.58	0.54	6.62	0.42	10.19	0.98	19.43	0.83	13.57	<b>0.45</b>	16.93	0.77	12.26
E2Former-V1	<u>0.67</u>	<b>8.90</b>	0.49	7.10	0.43	4.01	0.51	<b>5.63</b>	1.10	19.20	0.96	13.50	0.65	<b>10.20</b>	0.60	7.46
eSEN-Direct	-	-	-	-	-	-	-	-	-	-	-	-	-	-	0.56	10.98
eSEN-Cons.	-	-	-	-	-	-	-	-	-	-	-	-	-	-	<b>0.23</b>	<b>6.36</b>
E2V2-Direct	<b>0.65</b>	9.49	<b>0.46</b>	<u>4.59</u>	<b>0.28</b>	<u>2.40</u>	<b>0.33</b>	<u>5.63</u>	<b>0.56</b>	<u>13.37</u>	<b>0.70</b>	<u>7.43</u>	<u>0.63</u>	11.69	<u>0.53</u>	8.27
E2V2-Cons	0.69	<u>9.00</u>	<u>0.52</u>	<b>4.00</b>	<u>0.30</u>	<b>2.09</b>	<b>0.37</b>	<u>5.25</u>	<b>0.56</b>	<b>12.66</b>	<b>0.70</b>	<b>7.16</b>	0.66	<u>11.21</u>	0.57	7.80

ure 3a and Figure 3b, we compare the forward pass latency of our EAAS  $SO(2)$  tensor product against the standard e3nn  $SO(3)$  tensor product. The results verify that our method consistently outperforms the baseline as the number of tensor products increases. Notably, we observe a speedup of over  $6\times$  for both first-order and second-order operations. **Secondly**, we assess the system-level performance of our fused Equivariant Flash Attention Kernel. Figure 4 compares the throughput (TFLOPS) and peak memory usage of our kernel against a naive PyTorch implementation. As shown in Figure 4a and Figure 4b, our method demonstrates superior scalability: the TFLOPS rapidly increase with the number of neighbors and atoms before saturating at a high utilization rate, whereas the naive implementation remains at a consistently low throughput level. Consequently, we achieve an approximate  $20\times$  speedup. This trajectory indicates that our method effectively shifts the workload from being memory-bound to compute-bound as scale increases. Furthermore, as shown in Figure 4c and Figure 4d, our approach maintains a significantly lower memory footprint compared to the naive baseline, confirming its ability to scale efficiently to larger systems.

### 5.3. Performance comparison with related methods.

To evaluate the expressivity and generalizability of E2Former-V2, we benchmark it against recent equivariant architectures, including MACE (Batatia et al., 2022), eSEN (Passaro & Zitnick, 2023), UMA (Wood et al., 2025), and E2Former-V1 (Li et al., 2025).

**Firstly**, we evaluate generalization on the SPICE dataset. As shown in Table 1, E2Former-V2 achieves the lowest Energy and Force MAE across most subsets, including challenging regimes such as *Monomers*, *Dimers*, and *Solvated Amino Acids*. On *Dimers*, it reduces the Energy MAE by 48% relative to MACE-Large, demonstrating that the EAAS-based  $SO(2)$  formulation effectively captures high-order geometric interactions. **Secondly**, we assess scalability on the large-scale OMol25 dataset. As summarized in Table 2, E2Former-V2 remains competitive in this regime: the conservative variant achieves an aggregate Energy MAE of 1.27 meV/atom, matching eSEN-small and significantly outperforming UMA-S (3.62 meV/atom), confirming its suitability as an efficient backbone for large-scale molecular foundation models.

### 5.4. Comparison of inference speed.

To evaluate the inference efficiency of E2Former-V2, we benchmark it against a broad range of related architectures, including ORB-v3 (Rhodes et al., 2025), eSEN (Passaro & Zitnick, 2023), MACE (both Order-0 and Large variants) (Batatia et al., 2022), E2Former-V1 (Li et al., 2025), UMA-S (Wood et al., 2025), GotenNet (Aykent & Xia, 2025), Allegro (Musaian et al., 2022), and EquiformerV2 (Liao et al., 2023). As presented in Table 3, we measure the inference throughput (steps/s) across system sizes ranging from 1,000 to 100,000 atoms. To provide a comprehensive analysis, we compare methods in two distinct categories: the **Conservative** setting, where forces are derived via energy

Table 2. **OMol25 Performance.** Val-Comp results (Energy / Forces) across domains and total. **Bold** and underline denote the best and second-best performers. Shaded rows indicate our proposed E2Former-V2 variants.

DATASET	MODEL	VAL-COMP									
		BIOMOLECULES		ELECTROLYTES		METALS		ORGANICS		TOTAL	
		<i>E</i>	<i>F</i>	<i>E</i>	<i>F</i>	<i>E</i>	<i>F</i>	<i>E</i>	<i>F</i>	<i>E</i>	<i>F</i>
All	eSEN-sm-d	0.67	6.30	1.24	9.41	2.53	33.08	1.23	13.84	1.49	9.92
	eSEN-sm-cons	0.59	<b>4.61</b>	<b>1.01</b>	<b>8.08</b>	2.30	28.86	<b>0.84</b>	<b>11.11</b>	1.27	<b>8.25</b>
	UMA-S	0.53	5.69	2.69	11.65	4.63	37.85	1.00	13.15	3.62	12.02
	MACE-OMOL	1.76	6.05	2.15	10.87	2.15	24.51	2.31	23.70	1.84	10.10
	E2V2-Direct	0.70	6.30	1.58	10.12	2.62	26.46	1.29	20.71	<b>1.24</b>	9.55
	E2V2-Cons.	<b>0.52</b>	4.96	1.52	10.11	<b>2.18</b>	<b>24.40</b>	1.26	19.69	2.09	8.38

Table 3. **Inference Throughput Scaling.** Throughput (steps/s) is measured on a single H20 GPU. We compare methods in two categories: *Conservative* (forces via energy gradients,  $F = -\nabla E$ ) and *Direct* (forces via a dedicated force head). **Bold** and underline denote the best and second-best performers within each category. Shaded columns indicate our proposed E2Former-V2 variants.

SYSTEM SIZE $N$	CONSERVATIVE							DIRECT			
	ORB-V3	eSEN	MACE-0	MACE-L	E2V1	UMA-S	<b>E2V2-C</b>	GOTEN	ALLEGRO	EQUIV2	<b>E2V2-D</b>
<b>1k</b>	30.0	1.7	24.0	20.0	12.0	16.0	<b>38.9</b>	34.2	9.94	16.04	<b>140.0</b>
<b>10k</b>	3.70	OOM	2.90	OOM	1.28	1.60	<b>3.89</b>	3.41	OOM	OOM	<b>14.0</b>
<b>50k</b>	OOM	OOM	OOM	OOM	OOM	0.20	<b>0.60</b>	0.50	OOM	OOM	<b>2.62</b>
<b>100k</b>	OOM	OOM	OOM	OOM	OOM	0.10	<b>0.29</b>	0.27	OOM	OOM	<b>1.24</b>

gradients ( $F = -\nabla E$ ), and the **Direct** setting, where forces are predicted directly by a dedicated output head.

**Firstly**, we evaluate scalability under memory constraints. Prior equivariant Transformers such as EquiformerV2 and E2Former-V1, as well as high-order potentials like MACE-Large, quickly encounter out-of-memory (OOM) failures as system size grows, typically becoming infeasible beyond 10,000–50,000 atoms. In contrast, E2Former-V2 scales reliably to 100,000 atoms in both Conservative and Direct settings, demonstrating that our design effectively removes the memory bottlenecks that limit existing equivariant architectures. **Secondly**, E2Former-V2 exhibits a clear throughput advantage across all scales. In the Conservative setting, it consistently achieves the highest throughput, reaching 0.29 steps/s at 100,000 atoms—nearly  $3\times$  faster than the next-best UMA-S. This advantage is further amplified in the Direct setting: E2Former-V2 attains 140.0 steps/s at 1,000 atoms, an order-of-magnitude speedup over Allegro and EquiformerV2, and remains the only Transformer-based model that runs efficiently at 100,000 atoms, outperforming the specialized GotenNet by approximately  $4.5\times$ . Together, these results confirm the superior inference efficiency and scalability of E2Former-V2.

### 5.5. Molecular dynamics simulation.

We conducted molecular dynamics (MD) simulations using E2Former-V2 pretrained on the OMol25 dataset, comparing its performance against the MACE-OFF (Kovács et al., 2025). To validate physical accuracy, we benchmarked the Oxygen-Oxygen RDF from bulk water MD simulations (216 molecules) against the MACE baseline. As shown in Figure 5, E2Former-V2 demonstrates superior structural align-

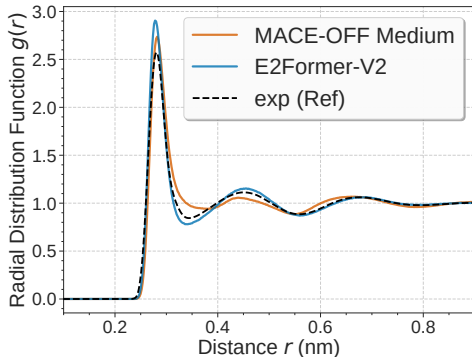


Figure 5. **Oxygen-Oxygen radial distribution function (RDF) comparison.** E2Former-V2 is compared against MACE-OFF and experimental data on bulk water.

ment with experimental data compared to MACE-OFF. This high-fidelity reproduction confirms E2Former-V2’s ability to accurately capture complex many-body interactions and hydrogen bond networks during long-term dynamics.

## 6. Conclusion

In this paper, we identify that the scalability of equivariant architectures is hindered by the memory bottlenecks of edge-centric tensor materialization. Then, we propose E2Former-V2, which integrates **Equivariant Axis-Aligned Sparsification (EAAS)** with a novel **On-the-Fly Equivariant Attention kernel**. This hardware-aware design strictly enforces node-centric computation and eliminates explicit edge tensors, thereby achieving linear activation memory. Experiments demonstrate that our method accelerates inference by **20x** while maintaining superior performance on molecular benchmarks.



## References

- Ayken, S. and Xia, T. GotenNet: Rethinking Efficient 3D Equivariant Graph Neural Networks. In *The Thirteenth International Conference on Learning Representations*, 2025. URL <https://openreview.net/forum?id=5wxQDtbMo>.
- Bartók, A. P., Payne, M. C., Kondor, R., and Csányi, G. Gaussian approximation potentials: The accuracy of quantum mechanics, without the electrons. *Physical review letters*, 104(13):136403, 2010.
- Bartók, A. P., Kondor, R., and Csányi, G. On representing chemical environments. *Physical Review B—Condensed Matter and Materials Physics*, 87(18):184115, 2013.
- Batatia, I., Kovacs, D. P., Simm, G. N. C., Ortner, C., and Csányi, G. MACE: Higher order equivariant message passing neural networks for fast and accurate force fields. In Oh, A. H., Agarwal, A., Belgrave, D., and Cho, K. (eds.), *Advances in Neural Information Processing Systems*, 2022. URL <https://openreview.net/forum?id=YPpSngE-ZU>.
- Batzner, S., Musaelian, A., Sun, L., Geiger, M., Mailoa, J. P., Kornbluth, M., Molinari, N., Smidt, T. E., and Kozinsky, B. E(3)-equivariant graph neural networks for data-efficient and accurate interatomic potentials. *Nature Communications*, 13(1), May 2022. ISSN 2041-1723. doi: 10.1038/s41467-022-29939-5. URL <http://dx.doi.org/10.1038/s41467-022-29939-5>.
- Dao, T. Flashattention-2: Faster attention with better parallelism and work partitioning. *arXiv preprint arXiv:2307.08691*, 2023.
- Dao, T., Fu, D., Ermon, S., Rudra, A., and Ré, C. Flashattention: Fast and memory-efficient exact attention with io-awareness. *Advances in neural information processing systems*, 35:16344–16359, 2022.
- Drautz, R. Atomic cluster expansion for accurate and transferable interatomic potentials. *Physical Review B*, 99(1): 014104, 2019.
- Eastman, P., Behara, P. K., Dotson, D. L., Galvelis, R., Herr, J. E., Horton, J. T., Mao, Y., Chodera, J. D., Pritchard, B. P., Wang, Y., Fabritiis, G. D., and Markland, T. E. Spice, a dataset of drug-like molecules and peptides for training machine learning potentials, 2022. URL <https://arxiv.org/abs/2209.10702>.
- Fey, M. and Lenssen, J. E. Fast graph representation learning with pytorch geometric, 2019. URL <https://arxiv.org/abs/1903.02428>.
- Fu, X., Wood, B. M., Barroso-Luque, L., Levine, D. S., Gao, M., Dzamba, M., and Zitnick, C. L. Learning smooth and expressive interatomic potentials for physical property prediction. *arXiv preprint arXiv:2502.12147*, 2025.
- Gasteiger, J., Becker, F., and Günnemann, S. Gemnet: Universal directional graph neural networks for molecules. *Advances in Neural Information Processing Systems*, 34: 6790–6802, 2021.
- Geiger, M. and Smidt, T. e3nn: Euclidean neural networks, 2022. URL <https://arxiv.org/abs/2207.09453>.
- Geiger, M., Smidt, T., M., A., Miller, B. K., Boomsma, W., Dice, B., Lapchevskyi, K., Weiler, M., Tyszkiewicz, M., Batzner, S., Madiseti, D., Uhrin, M., Frelsen, J., Jung, N., Sanborn, S., Wen, M., Rackers, J., Rød, M., and Bailey, M. Euclidean neural networks: e3nn, April 2022. URL <https://doi.org/10.5281/zenodo.6459381>.
- Hohenberg, P. and Kohn, W. Inhomogeneous electron gas. *Physical review*, 136(3B):B864, 1964.
- Ivanov, A., Dryden, N., Ben-Nun, T., Li, S., and Hoefler, T. Data movement is all you need: A case study on optimizing transformers, 2021. URL <https://arxiv.org/abs/2007.00072>.
- Jia, Z., Maggioni, M., Staiger, B., and Scarpazza, D. P. Dissecting the nvidia volta gpu architecture via microbenchmarking, 2018. URL <https://arxiv.org/abs/1804.06826>.
- Kohn, W. and Sham, L. J. Self-consistent equations including exchange and correlation effects. *Physical review*, 140(4A):A1133, 1965.
- Kovács, D. P., Moore, J. H., Browning, N. J., Batatia, I., Horton, J. T., Pu, Y., Kapil, V., Witt, W. C., Magdău, I.-B., Cole, D. J., and Csányi, G. Mace-off: Short-range transferable machine learning force fields for organic molecules. *Journal of the American Chemical Society*, 147(21):17598–17611, 2025. doi: 10.1021/jacs.4c07099.
- Levine, D. S., Shuaibi, M., Spotte-Smith, E. W. C., Taylor, M. G., Hasyim, M. R., Michel, K., Batatia, I., Csányi, G., Dzamba, M., Eastman, P., Frey, N. C., Fu, X., Gharakhanyan, V., Krishnapriyan, A. S., Rackers, J. A., Raja, S., Rizvi, A., Rosen, A. S., Ullissi, Z., Vargas, S., Zitnick, C. L., Blau, S. M., and Wood, B. M. The open molecules 2025 (omol25) dataset, evaluations, and models, 2025. URL <https://arxiv.org/abs/2505.08762>.

- Li, Y., Huang, L., Ding, Z., Wang, C., Wei, X., Yang, H., Wang, Z., Liu, C., Shi, Y., Jin, P., Qin, T., Gerstein, M., and Zhang, J. E2former: An efficient and equivariant transformer with linear-scaling tensor products, 2025. URL <https://arxiv.org/abs/2501.19216>.
- Liao, Y.-L. and Smidt, T. Equiformer: Equivariant graph attention transformer for 3d atomistic graphs. In *International Conference on Learning Representations*, 2023. URL <https://openreview.net/forum?id=KwmPfARgOTD>.
- Liao, Y.-L., Wood, B., Das, A., and Smidt, T. Equiformerv2: Improved equivariant transformer for scaling to higher-degree representations. *arXiv preprint arXiv:2306.12059*, 2023.
- Musaelian, A., Batzner, S., Johansson, A., Sun, L., Owen, C. J., Kornbluth, M., and Kozinsky, B. Learning local equivariant representations for large-scale atomistic dynamics, 2022. URL <https://arxiv.org/abs/2204.05249>.
- Passaro, S. and Zitnick, C. L. Reducing SO(3) convolutions to SO(2) for efficient equivariant GNNs. In Krause, A., Brunskill, E., Cho, K., Engelhardt, B., Sabato, S., and Scarlett, J. (eds.), *Proceedings of the 40th International Conference on Machine Learning*, volume 202 of *Proceedings of Machine Learning Research*, pp. 27420–27438. PMLR, 23–29 Jul 2023. URL <https://proceedings.mlr.press/v202/passaro23a.html>.
- Rhodes, B., Vandenhaute, S., Šimkus, V., Gin, J., Godwin, J., Duignan, T., and Neumann, M. Orb-v3: atomistic simulation at scale, 2025. URL <https://arxiv.org/abs/2504.06231>.
- Satorras, V. G., Hoogeboom, E., and Welling, M. E(n) equivariant graph neural networks, 2022. URL <https://arxiv.org/abs/2102.09844>.
- Schütt, K. T., Sauceda, H. E., Kindermans, P.-J., Tkatchenko, A., and Müller, K.-R. Schnet—a deep learning architecture for molecules and materials. *The Journal of Chemical Physics*, 148(24):241722, 2018.
- Schütt, K. T., Unke, O. T., and Gastegger, M. Equivariant message passing for the prediction of tensorial properties and molecular spectra, 2021. URL <https://arxiv.org/abs/2102.03150>.
- Shah, J., Bikshandi, G., Zhang, Y., Thakkar, V., Ramani, P., and Dao, T. Flashattention-3: Fast and accurate attention with asynchrony and low-precision. *Advances in Neural Information Processing Systems*, 37:68658–68685, 2024.
- Thomas, N., Smidt, T., Kearnes, S., Yang, L., Li, L., Kohlhoff, K., and Riley, P. Tensor field networks: Rotation- and translation-equivariant neural networks for 3d point clouds, 2018. URL <https://arxiv.org/abs/1802.08219>.
- Unke, O. T., Bogojeski, M., Gastegger, M., Geiger, M., Smidt, T., and Müller, K. R. SE(3)-equivariant prediction of molecular wavefunctions and electronic densities. In Beygelzimer, A., Dauphin, Y., Liang, P., and Vaughan, J. W. (eds.), *Advances in Neural Information Processing Systems*, 2021. URL <https://openreview.net/forum?id=auGY2UQfhSu>.
- Wang, Y., Li, S., He, X., Li, M., Wang, Z., Zheng, N., Shao, B., Wang, T., and Liu, T.-Y. Visnet: a scalable and accurate geometric deep learning potential for molecular dynamics simulation. *arXiv preprint arXiv:2210.16518*, 2022.
- Williams, S., Waterman, A., and Patterson, D. Roofline: an insightful visual performance model for multicore architectures. *Commun. ACM*, 52(4):65–76, April 2009. ISSN 0001-0782. doi: 10.1145/1498765.1498785. URL <https://doi.org/10.1145/1498765.1498785>.
- Wood, B. M., Dzamba, M., Fu, X., Gao, M., Shuaibi, M., Barroso-Luque, L., Abdelmaqsoud, K., Gharakhanyan, V., Kitchin, J. R., Levine, D. S., et al. Uma: A family of universal models for atoms. *arXiv preprint arXiv:2506.23971*, 2025.
- Wulf, W. A. and McKee, S. A. Hitting the memory wall: implications of the obvious. *SIGARCH Comput. Archit. News*, 23(1):20–24, March 1995. ISSN 0163-5964. doi: 10.1145/216585.216588. URL <https://doi.org/10.1145/216585.216588>.

## A. Latency Measurement Details

Figure 1 reports end-to-end forward latency of the same sparse attention pipeline (QK score computation + softmax over neighbors + value aggregation) under a fixed neighbor budget  $K$  while sweeping the number of atoms  $N$ . Unless otherwise noted, the benchmark uses fp32 on a single GPU, with  $K = 64$ ,  $H = 16$ , and  $N \in \{128, 512, 2048, 8192, 32768\}$ .

**Curve definitions.** **Traditional EGNs** corresponds to a PyTorch edge-centric sparse implementation that explicitly gathers neighbor keys/values, materializing intermediate tensors of shape  $N \times K \times H \times D$  (keys) and  $N \times K \times H \times C$  (values), followed by QK reduction, softmax over the neighbor dimension, and a weighted value reduction.

**FlashAttention** corresponds to a sparse masked-attention baseline implemented using PyTorch `scaled_dot_product_attention` with a pre-built attention mask encoding the same  $K$ -neighbor pattern. The mask is constructed once per  $N$  and reused across timing iterations so that mask construction is not included in the reported latency.

**Ours** corresponds to the proposed fused sparse implementation, where QK and value aggregation are computed using custom kernels, and the reduction over neighbors is performed on the fly without explicitly materializing edge-level intermediate tensors.

**Timing protocol.** For each  $N$ , we generate random inputs  $(q, k, h')$  and neighbor indices  $\mathbf{I} \in \mathbb{Z}^{N \times K}$ . We run 10 warmup iterations followed by 50 timed iterations. Each iteration synchronizes the GPU (`torch.cuda.synchronize()`) before reading the wall-clock time. The plotted latency is the mean over timed iterations.

**Reference implementation snippets.** The following code sketch summarizes the three implementations used to generate Figure 1.

```
# Traditional EGNs (PyTorch sparse): explicit gather + materialization
gk = key[idx].view(N, K, H, D)           # materialize N x K x H x D
scores = (query[:,None] * gk).sum(-1)     # N x K x H
alpha = softmax(scores, dim=1)            # N x K x H
gv = value[idx].view(N, K, H, C)         # materialize N x K x H x C
out = (alpha[:,None] * gv).sum(1)         # N x H x C

# FlashAttention (sparse): SDPA with pre-built K-neighbor mask
mask = build_mask_from_idx(idx)           # built once, not timed
out = scaled_dot_product_attention(q, k, v, attn_mask=mask)

# Ours: fused sparse kernels (QK + V) with on-the-fly reduction
scores = triton_sparse_qk(query, key, idx, gate, scale) # N x K x H
alpha = softmax(scores, dim=1)
out = triton_sparse_v(value, alpha, idx) # N x H x C
```

## B. Derivation of the EAAS Re-indexing Operator

This appendix provides the explicit form and derivation of the re-indexing operator  $\mathcal{P}$  introduced in Definition 4.2 and used in Proposition 4.3. All derivations are exact and preserve  $\text{SO}(3)$  equivariance.

### B.1. Deriving the EAAS Re-indexing Rule

This subsection explains how the sparse re-indexing rule used to define  $\mathcal{P}$  arises from standard Clebsch–Gordan (CG) structure after (i) aligning  $\vec{r}$  to the  $z$ -axis and (ii) expressing features in the real  $\text{SO}(3)$  basis adopted throughout this paper.

**Complex vs. real CG conventions.** Many selection rules are most conveniently stated in the complex (physics) spherical-harmonic basis. To make this explicit, we denote the CG coefficients in the complex basis by  $\bar{C}_{(\ell_i, m_i), (\ell_f, m_f)}^{(\ell_o, m_o)}$ , and the CG coefficients in our real  $\text{SO}(3)$  basis by  $C_{(\ell_i, m_i), (\ell_f, m_f)}^{(\ell_o, m_o)}$ . The two conventions are related by a fixed change-of-basis within

each degree  $\ell$  that mixes the pair of orders  $\{m, -m\}$ .

Concretely, let  $z_m^{(\ell)}$  denote the complex basis and  $x_m^{(\ell)}$  the real basis used in the paper. They are related (for each  $\ell$ ) by

$$x_m^{(\ell)} = \begin{cases} \frac{i}{\sqrt{2}} \left( z_m^{(\ell)} - (-1)^m z_{-m}^{(\ell)} \right), & m < 0, \\ z_0^{(\ell)}, & m = 0, \\ \frac{1}{\sqrt{2}} \left( z_m^{(\ell)} + (-1)^m z_{-m}^{(\ell)} \right), & m > 0. \end{cases} \quad (19)$$

This change-of-basis is fixed (input-independent) and depends only on  $(\ell, m)$ .

**Alignment implies  $m_f = 0$ .** Let  $R \in \text{SO}(3)$  align the global  $z$ -axis with  $\vec{r}$ . By Lemma 4.1, in the aligned frame the geometric encoding has only the zero-order component:

$$\mathcal{R}_m^{(\ell_f)}(R\vec{r}) \propto \delta_{m,0}, \quad \text{i.e.,} \quad m_f = 0. \quad (20)$$

Therefore, the CG contraction in the aligned frame always couples with  $(\ell_f, 0)$ .

**Selection rule in the complex basis.** In the complex basis, CG coefficients satisfy the standard order constraint:

$$\bar{C}_{(\ell_i, m_i), (\ell_f, m_f)}^{(\ell_o, m_o)} \neq 0 \quad \Rightarrow \quad m_o = m_i + m_f. \quad (21)$$

With  $m_f = 0$ , this implies that in the complex basis only terms with  $m_o = m_i$  can contribute:

$$\bar{C}_{(\ell_i, m_i), (\ell_f, 0)}^{(\ell_o, m_o)} \neq 0 \quad \Rightarrow \quad m_o = m_i. \quad (22)$$

Moreover, the complex CG coefficients obey the symmetry relation

$$\bar{C}_{(\ell_i, m_i), (\ell_f, m_f)}^{(\ell_o, m_o)} = (-1)^{\ell_i + \ell_f + \ell_o} \bar{C}_{(\ell_i, -m_i), (\ell_f, -m_f)}^{(\ell_o, -m_o)}. \quad (23)$$

Setting  $m_f = 0$  and using  $m_o = m_i$  yields, for any  $m$ ,

$$\bar{C}_{(\ell_i, m), (\ell_f, 0)}^{(\ell_o, m)} = (-1)^{L_\Sigma} \bar{C}_{(\ell_i, -m), (\ell_f, 0)}^{(\ell_o, -m)}, \quad L_\Sigma := \ell_i + \ell_f + \ell_o. \quad (24)$$

**Change-of-basis induces parity-dependent sparsity.** Equation (19) mixes the  $\{m, -m\}$  pair when passing from the complex basis to the real basis. For any fixed  $m \neq 0$ , consider the  $2 \times 2$  block of coefficients associated with the ordered pair  $\{-m, m\}$  (input and output). Using Eq. (22)–(24) and applying the change-of-basis on both the input and output irreps yields a parity-dependent collapse:

- If  $L_\Sigma$  is even, the real-basis coupling is diagonal in the pair  $\{-m, m\}$ , i.e., only the mapping  $m_i = m_o$  survives.
- If  $L_\Sigma$  is odd, the real-basis coupling becomes off-diagonal in the pair  $\{-m, m\}$ , i.e., only the mapping  $m_i = -m_o$  survives, and the surviving entry acquires a fixed sign factor depending on  $m_o$ .

Under our convention, this fixed sign appears as the factor  $-2(-1)^{m_o}$ .

The case  $m = 0$  is consistent with the above rule: Eq. (24) implies that the  $m_o = 0$  component vanishes when  $L_\Sigma$  is odd.

**Resulting re-indexing rule.** Combining the above observations, the action of  $\mathcal{P}$  in the aligned frame reduces to a deterministic re-indexing (within each  $\ell$ -block) with no dense summation over magnetic indices:

$$(\mathcal{P}(\tilde{h}))_{m_o}^{(\ell_o)} = \left[ \begin{cases} C_{(\ell_i, m_i), (\ell_f, 0)}^{(\ell_o, m_o)} \tilde{h}_{m_i}^{(\ell_i)}, & \text{if } L_\Sigma \text{ is even,} \\ -2(-1)^{m_o} C_{(\ell_i, -m_i), (\ell_f, 0)}^{(\ell_o, m_o)} \tilde{h}_{-m_i}^{(\ell_i)}, & \text{if } L_\Sigma \text{ is odd,} \end{cases} \right], \quad (25)$$

where  $L_\Sigma = \ell_i + \ell_f + \ell_o$ , and the repeated index  $m_i$  is implicitly summed over. This is exactly the re-indexing structure used in Definition 4.2 and Proposition 4.3.



## B.2. Proof of Proposition 4.3

We derive the aligned-frame form of  $\mathcal{P}$  from the Clebsch–Gordan contraction underlying the  $\text{SO}(3)$ -equivariant tensor product.

**Commuting the rotation.** Consider the  $\text{SO}(3)$ -equivariant tensor product between node features  $h^{(\ell_i)}$  and geometric encodings  $\mathcal{R}^{(\ell_f)}(\vec{r})$ . By equivariance, for any rotation  $R \in \text{SO}(3)$ ,

$$h \otimes \mathcal{R}(\vec{r}) = D_{R^{-1}} \left( D_R h \otimes D_R \mathcal{R}(\vec{r}) \right). \quad (26)$$

Let  $\tilde{h} = D_R h$  denote the node features expressed in the aligned frame.

**Pole sparsity.** Choosing  $R$  such that the global  $z$ -axis is aligned with  $\vec{r}$ , Lemma 4.1 implies

$$\mathcal{R}_m^{(\ell_f)}(R\vec{r}) \propto \delta_{m,0}. \quad (27)$$

Thus, the geometric encoding contains only the zero-order component  $m_f = 0$  in the aligned frame.

**Clebsch–Gordan expansion.** Projecting the tensor product in Eq. (26) to output degree  $\ell_o$  and order  $m_o$  yields

$$(h \otimes \mathcal{R}(\vec{r}))_{m_o}^{(\ell_o)} = \sum_{m_i=-\ell_i}^{\ell_i} \tilde{h}_{m_i}^{(\ell_i)} C_{(\ell_i, m_i), (\ell_f, 0)}^{(\ell_o, m_o)}. \quad (28)$$

**Parity selection rule.** The Clebsch–Gordan coefficients in Eq. (28) obey a parity selection rule. Let  $L_\Sigma = \ell_i + \ell_f + \ell_o$ . If  $L_\Sigma$  is even, the coefficient is non-zero only when  $m_i = m_o$ . If  $L_\Sigma$  is odd, the coefficient is non-zero only when  $m_i = -m_o$ , up to a fixed sign convention, which in our notation appears as the factor  $-2(-1)^{m_o}$  in Eq. (25). All other combinations vanish.

Substituting this rule into Eq. (28) recovers exactly the operator form in Eq. (25), completing the proof.

## B.3. Concrete Examples

We illustrate the re-indexing operator for low-degree cases.

$\ell_i = 1, \ell_f = 1, \ell_o = 0$ . Here  $L_\Sigma = 2$  is even, and the only output order is  $m_o = 0$ . The re-indexing rule yields

$$(\mathcal{P}(\tilde{h}))_0^{(0)} = C_{(1,0), (1,0)}^{(0,0)} \tilde{h}_0^{(1)}.$$

Thus, the scalar output depends only on the  $m = 0$  component of the input.

$\ell_i = 1, \ell_f = 1, \ell_o = 1$ . Here  $L_\Sigma = 3$  is odd. The re-indexing rule maps each output order to the opposite input order:

$$(\mathcal{P}(\tilde{h}))_{m_o}^{(1)} = -2(-1)^{m_o} C_{(1, -m_o), (1,0)}^{(1, m_o)} \tilde{h}_{-m_o}^{(1)}.$$

The  $m_o = 0$  component vanishes due to the Clebsch–Gordan coefficient, while the  $m_o = \pm 1$  components are obtained by swapping the corresponding input orders.

These examples illustrate that  $\mathcal{P}$  acts as a deterministic re-indexing with scaling, rather than a dense summation, within each representation block.

## C. Datasets

This appendix summarizes the two datasets used in our evaluation: SPICE and OMol25.

**SPICE (Small-molecule/Protein Interaction Chemical Energies).** SPICE focuses on quantum-mechanical energetics relevant to medicinal chemistry settings, particularly small molecules in protein-like environments and related non-covalent interactions. The dataset contains over 1.1M conformations spanning drug-like small molecules, dimers, dipeptides, and solvated amino acids, covering both neutral and charged species and multiple interaction motifs. For each conformation, SPICE provides high-quality quantum chemical labels including energies and forces (and additional molecular properties such as multipole moments and bond orders), computed at the  $\omega$ B97M-D3(BJ)/def2-TZVPPD level of theory.

**OMol25 (Open Molecules 2025).** OMol25 is a large-scale, high-accuracy quantum chemistry dataset designed for training and evaluating foundation-scale molecular models across broad chemical space. It contains more than 100M DFT single-point calculations at the  $\omega$ B97M-V/def2-TZVPD level of theory, comprising roughly 83M unique molecular systems. OMol25 provides exceptional chemical and elemental diversity (including a wide range of intra- and intermolecular interactions, conformers, variable charge/spin states, and reactive structures), and includes systems up to approximately 350 atoms.

## D. Inference throughput benchmark setup

This section describes the experimental setup used to produce Table 3.

**Hardware and metric.** All throughput numbers are measured on a single NVIDIA H20 GPU. We report *throughput* as steps per second (QPS), computed as  $\text{QPS} = \text{steps} / \text{time}$ , where *time* is the wall-clock duration of a fixed number of forward passes.

**System generation.** Following the UMA benchmark methodology, synthetic molecular systems are generated using an FCC carbon crystal from ASE. For a target atom count  $N$ , we construct an FCC carbon supercell and uniformly sample  $N$  atoms without replacement. We use a lattice constant  $a = 3.8$ , which yields approximately  $\sim 50$  neighbors per atom under a  $6 \text{ \AA}$  cutoff in the original UMA setting. We evaluate system sizes  $N \in \{1k, 10k, 50k, 100k\}$ . Inputs are converted to the model format using the same batching pipeline (`collate_fn`) as in training.

**Model invocation and force modes.** We benchmark inference in two categories: *Conservative* models compute forces via energy gradients,  $F = -\nabla E$ , which requires autograd through the energy head. *Direct* models predict forces with a dedicated force head. For the Direct category, we disable autograd-force computation (`AutoGradForce=False`) and report the runtime of direct force prediction. All runs use `model.eval()` and `torch.no_grad()`.

**Timing protocol.** For each system size  $N$ , we run 10 warmup iterations followed by 10 timed iterations. Timing uses `timeit.timeit` over the complete forward call, with `torch.cuda.synchronize()` inside the timed function to ensure accurate GPU measurement. We report the average time per step and QPS.

**Memory reporting and OOM handling.** We reset peak CUDA memory statistics before benchmarking each  $N$  (`torch.cuda.reset_peak_memory_stats()`) and report the peak allocated memory when available. If an evaluation fails due to out-of-memory (OOM) or other runtime errors, the corresponding entry is marked as OOM in Table 3.

**Preprocessing details.** All inputs are generated with periodic boundary conditions (PBC) available from ASE but are disabled during benchmarking (`pbcs` set to zero) to match the reported configuration. We also force sparse attention in E2Former-V2 by setting `flatten_atoms.threshold=0`. Additional configuration overrides used for the E2Former-V2 benchmarks include: `tp_type="QK_alpha+triton"`, `with_cluster="mixcluster"`, and `pbcs_expanded_num_cell_per_direction=1`.